Research Article Vol. 34, No. 4 / 23 Feb 2026 / Optics Express 6721
Optics EXPRESS

Elasto-optic transduction in polymer-cladded silicon microring arrays for real-time 2D force mapping

SAHAR SAFARLOO,[1,2,*] R. TUFAN ERDOGAN,[2] WOUTER J. WESTERVELD,[2] AMIR A. ZADPOOR,[1] PETER G. STEENEKEN,[2] AND MOHAMMAD J. MIRZAALI[1]

[1]Department of Biomechanical Engineering, Faculty of Mechanical Engineering, Delft University of Technology (TU Delft), Mekelweg 2, 2628 CD, Delft, The Netherlands
[2]Department of Precision and Microsystems Engineering, Faculty of Mechanical Engineering, Delft University of Technology, Mekelweg 2, Delft, 2628 CD, The Netherlands
[*]s.safarloo@tudelft.nl

Abstract: Real-time mapping of small forces with micrometer resolution is essential for studying soft and biological matter. However, existing techniques are slow, limited in spatial sampling or require non-planar substrates that can perturb cell behavior. Here we present silicon sensor arrays for rapid surface force mapping that operate using the elasto-optically induced wavelength shift in thin polymer-cladded optical ring resonators. Using a nano-indenter, we demonstrate that the sensor array reaches a force resolution down to 12 μN and shows a linear response. We present both a five-ring linear array and a 10×5 two-dimensional array at 15 μm pitch, and demonstrate the feasibility of localization and force mapping of a spherical nanoindentation tip. Combined measurement of forces by nano-indenter and the optical ring resonator sensor presents a methodology for calibrating this type of photonic force sensor. Moreover, good correspondence between measurements and finite element simulations provides evidence for the proposed operation mechanism. The shown combination of biocompatible claddings, strong opto-mechanical coupling, and foundry-ready photonics, presents a route towards scalable, real-time force mapping for soft-matter metrology, tactile interfaces, and *in vitro* mechanobiology.

1. Introduction

To understand cell mechanics and its link to cell functions, biomedical researchers are interested in high sensitivity, real-time, simultaneous measurement, and spatial mapping of forces exerted by biological tissue on surfaces with micrometer-scale resolution [1]. Although there are several established techniques for measuring forces at these scales, none of them can satisfy these criteria simultaneously. Atomic force microscopy (AFM) is a well-established method that offers nanoscale resolution. However, it is often limited by slow imaging speeds and is not suitable for dynamic measurements in complex biological environments [2,3]. Optical tweezers, another established technique, provide excellent force control but are limited in their ability to measure forces at multiple locations within a sample simultaneously [4,5]. Newer techniques have emerged to address these limitations. For instance, traction force microscopy (TFM) coupled with advanced computational methods enables high-resolution mapping of cellular forces on deformable substrates, offering insights into cell-matrix interactions [6]. However, its resolution is limited by the density of fiducial markers and inverse problem regularization [7]. The use of micro and nano pillars has allowed two-dimensional measurement of lateral forces down to piconewtons [8], but the topography of these pillars can change cell behavior and bias adhesion

#584401 https://doi.org/10.1364/OE.584401
Journal © 2026 Received 11 Nov 2025; revised 30 Jan 2026; accepted 5 Feb 2026; published 17 Feb 2026

Optics EXPRESS

localization [9]. Therefore, force sensing on a flat surface is preferred with an integrated readout, which allows the simultaneous measurement of multiple locations. Furthermore, recent advances in fiber optic force sensors provide minimally invasive options for measuring forces in confined spaces; their spatial resolution is bounded by the number and placement of sensing sites (often a single or a few points at the tip of the instrument), making wide field mapping challenging [10].

Beyond these techniques, a rapidly growing class of (nano)materials-based optical force sensors enables fully remote readout with diffraction-limited spatial resolution. Luminescent force probes based on rare-earth-doped micro- and nanocrystals transduce local stress into changes in emission spectra or intensity, allowing piconewton-micronewton force sensing through far-field microscopy and spectroscopy in three-dimensional environments [11,12]. Pressure-sensitive mechanoluminescent phosphors further provide highly responsive optical manometers for mapping stress with optical access only [13]. In parallel, stretchable optoelectronic devices that integrate colloidal quantum dots or related nanomaterials with elastomeric substrates demonstrate skin-like, conformal sensors for physiological pressure and force monitoring [14]. These nanomaterials-based approaches excel in remote readout and nanoscale spatial resolution, but typically rely on dispersed particles or localized elements rather than a continuous, planar array with integrated photonic readout for wide-field surface force mapping, as pursued in this work. Table 1 provides a summary of the techniques. These limitations highlight the need for alternative sensing methodologies that can overcome the challenges mentioned above.

Silicon photonics allows integration of many (>1000) small ($\approx 5\,\mu$m) and highly sensitive components in a single microchip. Combining silicon photonics with Micro-electro-mechanical systems (MEMS) is an active area of research [15], and ultra-sensitive silicon-photonic mechanical sensors have been demonstrated [16]. However, fabrication of mechanical membranes over silicon photonic waveguides is both technically challenging and costly. Moreover, most existing silicon-photonic force or ultrasound sensors operate by detecting geometrical deformations of rigid silicon structures (e.g., beams, membranes, or rings) that perturb the guided mode and shift optical resonances; examples include ring-on-membrane and strain-coupled ring sensors [17,18]. Polymer claddings have previously been employed to enhance the mechano-optic response of silicon-photonic microring resonators, particularly for acoustic/ultrasound pressure detection (e.g., BCB- or polymer-coated resonators for ultrasound and optoacoustic sensing [19–21]). In addition, our earlier work [22] leveraged a related polymer-cladding strategy.

Here, we extend this polymer-cladded resonator concept to the quasi-static, localized micro-force regime by realizing a spatially resolved force sensor comprising a 10×5 silicon photonic ring resonator array (PRRA) clad with a 3 µm-thin polydimethylsiloxane (PDMS) coating. Localized mechanical loading of the PDMS induces a photoelastic change in its refractive index [23], which modifies the effective index of the underlying waveguide and shifts the resonance wavelength of each ring. To improve the PRRA sensitivity, we use a PDMS cladding with an optimized optomechanical response recently developed in our group [22]. A key contribution of this work is the *calibration methodology*: we combine a calibrated, microscope-aligned nano-indenter with a wavelength-division multiplexed ring readout of the ring array via a shared bus waveguide. The nano-indenter allows calibration of the position dependent force sensitivity of the sensor array. It might also be used as a mechanical stimulus for biological samples [24] while they are being monitored.

Our proposed PRRA-force sensor concept, with its potential for high spatial resolution, sensitivity, and real-time measurement capabilities, represents a significant step towards advancing our understanding of biological mechanics. These attributes open routes to: *live-cell mechanotransduction assays* on flat, optically accessible substrates (e.g., adhesion dynamics, nuclear mechanics) [9]; spatially resolved probing of *soft-tissue and organoid interfaces* on biocompatible coatings [25]; and *tactile and robotic skins* that benefit from dense, low-profile arrays [26].

Optics EXPRESS

Table 1. Comparison of techniques for cellular force measurement

Technique	Advantages	Limitations
Atomic force microscopy (AFM)	High force sensitivity; nanoscale spatial resolution	Slow imaging; less suited to dynamic/complex biological environments [2,3]
Optical tweezers	Excellent force control; single-molecule sensitivity	Localized measurements; limited multiplexing [4,5]
Traction force microscopy (TFM)	Mapping of cellular forces on deformable substrates; cell–matrix insights	Resolution limited by marker density and inverse-problem regularization; [6,7]
Micro/nanopillars	Piconewton sensitivity; 2D lateral force readout	Pillar topography perturbs cell behavior/adhesion localization [8,9]
Fiber-optic force sensors	Minimally invasive; suitable for confined spaces	Limited spatial sampling (few sensing sites); difficult wide-field mapping [10]
Nanomaterials-based luminescent and stretchable force sensors	Remote optical readout; high force sensitivity; diffraction-limited spatial resolution; can operate in 3D or on soft, curved substrates	Typically rely on dispersed particles or localized elements rather than continuous planar arrays; require optical access and spectral calibration; wide-field planar mapping is non-trivial [11–14]
This work	Flat surface, integrated optical readout; simultaneous, real-time measurement at multiple sites; micrometer-scale spatial mapping	Still under development; sensitivity/resolution to be benchmarked against biological use cases

2. Materials and methods

2.1. Force characterization setup

The core of the photonic force sensor is based on silicon photonic microring resonators (MRRs), as illustrated in Fig. 1(a). Each sensor consists of one or more sensing MRRs and a reference MRR, positioned at a distance to remain unaffected by applied forces. The reference MRR serves as a control to account for temperature or other non-mechanical drifts. All rings are evanescently coupled to a shared bus waveguide. The photonic structures are fabricated on a silicon-on-insulator (SOI) substrate (2 μm), with the waveguides and microrings defined in the top silicon layer. The entire chip is then coated with a thin layer of soft PDMS (3 ± 1 μm), which serves as a mechanically responsive cladding. Figure 1(b) shows a schematic of the waveguide with a nominal cross-section of 450 nm × 220 nm.

To apply precise, localized forces with submicrometer positional control, we integrate a camera-compatible nanoindenter with our photonic readout. The system provides calibrated loading with spherical glass tips, on-axis optical access for alignment/imaging, and programmable loading profiles (Fig. S1 of the supplementary document). During experiments, a nanoindenter tip applies localized pressure onto the PDMS layer directly above the sensing MRR. Figure 1(c) shows an illustration of the load profile where the indenter applies a specified load value and waits

Optics EXPRESS

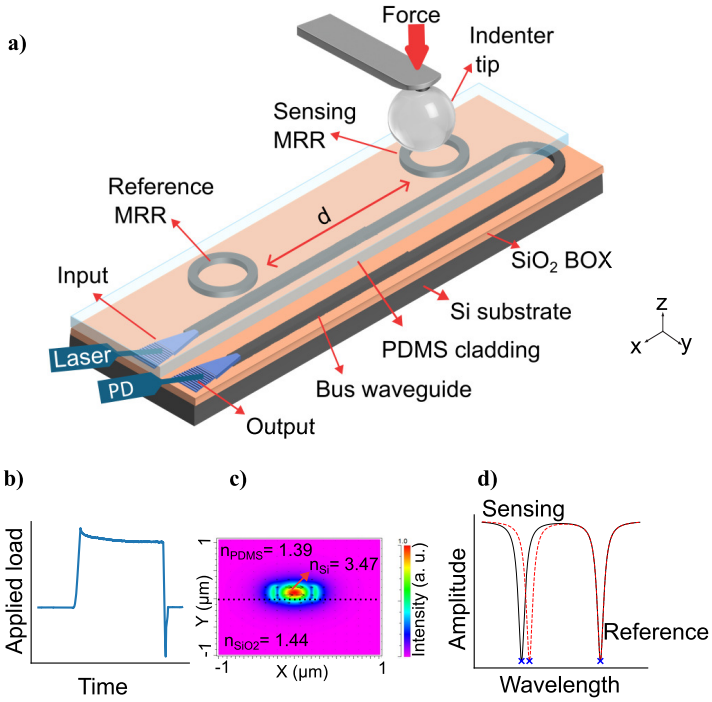

Fig. 1. a) A schematic drawing of the photonic force sensor based on dual microring resonators (MRRs), where an external force applied *via* an indenter tip pressurized the PDMS cladding over the sensing MRR. b) Cross-section of waveguide. c) An illustration of the load profile used in measurements (step–hold–release). d) Readout principle: Black line shows the spectrum before load application. Applied force causes a shift in the resonance dip of the sensing ring (red dashed line).

for a few seconds for the optical measurements to be done, and then releases. We synchronize the load application with tunable-laser wavelength sweeps and capture the transmission spectra to determine the wavelength shift of the absorption peak at the optical resonance of the MRR. In our setup, a single force "frame" corresponds to one full wavelength sweep of the tunable laser, during which the through-port transmission spectrum is recorded and the resonance wavelengths of all rings on a given bus are extracted. The maximum sweep speed of the laser is 50 nm/s, while the free spectral range (FSR) of the microrings is approximately 20 nm. Restricting the sweep to one FSR is sufficient to capture all resonances on a bus, so that the optical interrogation time for one 1×10 array is ~ 0.4 s, with a modest additional overhead for data transfer and fitting. The longer step–hold–release durations used in the present experiments are therefore chosen for convenience and do not reflect a fundamental limitation of the photonic readout.

As shown schematically in Fig. 1(d), the sensing mechanism relies on tracking the through-port transmission spectrum. A shift in the resonance dip of the sensing MRR can be caused by both applied force and temperature. Subtracting the shift of the reference MRR from the shift of the sensing MRR isolates the force-induced shift and suppresses drift and noise due to temperature and other external sources. This approach is seen to substantially improve the stability of the signal. In all measurements, the sensing and reference MRRs are interrogated within the same wavelength sweep, so that temperature and other common-mode drifts are sampled concurrently with the applied load. No separate temperature-interrogation step is required; instead, the instantaneous resonance shift of the reference ring provides a real-time estimate of the non-mechanical drift that is subtracted from the sensing-ring shift.

Optics EXPRESS

2.2. Force calibration measurements

We used a commercial nano-indentation instrument (Chiaro, Optics11 B.V., Netherlands) to apply localized forces at controlled values directly above the sensing microring resonator. The probe consisted of a spherical *glass* tip with a radius $R = 11\mu$m attached to a compliant cantilever with nominal spring constant $k = 199$ N/m. The applied force was determined from the cantilever deflection using $F = k\,\delta$, where δ denotes the cantilever deformation, measured precisely by optical interferometry. The built-in calibration of the instrument (performed before each measurement session) was used to verify k and the sensitivity to deflection. The tip position relative to the sensing microring was visualized with an angled camera (CS165MU1; Thorlabs Inc., USA), providing lateral placement within ~ 1 μm.

Indentation was carried out under quasi-static conditions using a step-and-hold load profile. At each load step the tip was held stationary for the duration of one full laser wavelength sweep, during which the transmission spectrum was recorded. Indentation depth was computed as piezo displacement minus cantilever deflection.

For optical coupling, a two-channel fiber array was aligned to the bus grating couplers (single-mode input for TE optical mode excitation; multimode output for collection). To calibrate the sensor, forces ranging from 0 to 80 μN were applied to the sensing ring. At each step, we recorded the optical transmission spectrum using a tunable laser (81940A; Keysight Technologies, USA) sweep. The light was detected using a photodetector (1811-FC-AC; Newport Corporation, USA) with a DC intensity being recorded. These outputs were digitized using an oscilloscope (RTA4004; Rohde & Schwarz GmbH & Co. KG, Germany).

The resonance wavelength of the sensing ring was extracted by fitting a Lorentzian profile to the transmission dip. From the same Lorentzian fits we also extract the full width at half maximum $\Delta\lambda_{\mathrm{FWHM}}$ and calculate the optical quality factor as $Q = \lambda_r/\Delta\lambda_{\mathrm{FWHM}}$. To compensate for thermal and environmental drifts, the resonance shift of the reference ring was subtracted from that of the sensing ring. This differential measurement isolates the shift caused by the applied force alone. The entire calibration process was repeated three times, and the average resonance shift along with standard deviation was computed for each force level to evaluate repeatability.

2.3. Chip design and fabrication

The microring arrays and routing were laid out in *Synopsys OptoDesigner*. Sensing and reference rings had nominal radii around 3.95 −4.05 μm; small radius variations were used to distribute the resonances for wavelength-division multiplexed readout. We chose the ring radii so that N+1 resonances would be equally spaced within one FSR, but we implement only N rings. The unused 'slot' appears as a missing resonance in the spectrum, which serves as a marker that fixes the ordering and lets us map each dip uniquely to its ring position along the bus. The force-induced shifts are much smaller than the slot spacing, so this mapping remains unchanged during measurements. Coupling gaps were designed for near-critical coupling at 1550 nm; the final coupling condition for each ring was verified from the measured transmission spectra.

Fabrication was performed as a full-wafer custom run at the CORNERSTONE silicon photonics foundry (University of Southampton, UK) on a standard silicon-on-insulator (SOI) platform (device Si thickness ~220 nm on ~2 μm buried oxide). Wafers were supplied without a deposited upper oxide cladding, leaving the photonic layer accessible for post-processing. After dicing, dies were solvent-cleaned and dried before polymer cladding.

2.4. PDMS cladding fabrication

We used Sylgard 184 silicon elastomer kit (DOW Inc., USA) as the cladding material. The elastomer consists of a base (Part A) and a curing agent (Part B); these were mixed for 5 min at a 1:30 (B:A) ratio, which was previously identified as optimal in another study of ours [22]. The uncured mixture was degassed in a vacuum desiccator for 30 min and then spin-coated onto

Optics EXPRESS

the photonic chips at 6000 rpm for 10 min. The coated samples were cured at 80°C for 2 h and allowed to cool to room temperature before measurement. The PDMS thickness, measured by white-light interferometry, was found to be 2.9 ± 0.23 μm.

2.5. Theory and elasto-optic model for polymer-cladded silicon photonic force sensors

The force detection performance of a silicon photonic resonator can be characterized by its resonance wavelength sensitivity, $S_{\lambda_{\text{res}}}$, which describes how the resonance wavelength shifts in response to an applied force. This shift arises from two primary mechanisms: (i) a change in the effective refractive index of the guided optical mode via the photoelastic (elasto-optic) effect, and (ii) deformation of the resonator structure and its waveguide geometry. In our device, the evanescent field penetrates less than 1 μm into the PDMS cladding. Therefore, for low-indentation regime used in this study and with a 3 μm PDMS cladding thickness, the PDMS deformation does not significantly interact with the optical mode. The device is therefore expected to respond predominantly to elasto-optic refractive index changes in the PDMS layer via mechanism (i), with negligible contribution from cladding-layer geometry changes caused by applied load. Under these conditions, the resonance wavelength sensitivity can be expressed as [27]:

$$S_{\lambda_{\text{r}}} = \frac{\partial \lambda_{\text{r}}}{\partial F} = \frac{\lambda_r}{n_{\text{g}}} \frac{\partial n_{\text{eff}}}{\partial F} \tag{1}$$

where λ_r is the resonance wavelength, F is the applied load, n_{g} is the waveguide group index, and n_{eff} is the effective refractive index of the guided mode. n_{g} is determined by the waveguide design. It can be evaluated from the material properties and waveguide geometry using the finite element method (FEM) simulations. We can further expand the second term on the right-hand side of Eq. (1), which represents the change in the effective refractive index of the guided mode in response to an applied force. The effective refractive index of a waveguide mode is determined by the waveguide geometry, wavelength, and the refractive indices of its materials. For a cladding material with a high elasto-optic effect, this term can be expressed as:

$$\frac{\partial n_{\text{eff}}}{\partial F} = \frac{\partial n_{\text{eff}}}{\partial n_{\text{clad}}} \frac{\partial n_{\text{clad}}}{\partial F} \tag{2}$$

where n_{clad} is the refractive index of the cladding material. The first term on the right-hand side describes how the optical mode field interacts with the cladding. Its value is determined by the refractive indices of the materials and the geometry of the waveguide. The second term on the right-hand side shows that the applied load changes the cladding refractive index as it builds stress in the material. The stress in the core and cladding material directly changes the local refractive index due to the elasto-optic effect, which can be defined as [28]:

$$n_x \approx n_0 - C_1\sigma_x - C_2(\sigma_y + \sigma_z), \tag{3a}$$

$$n_y \approx n_0 - C_1\sigma_y - C_2(\sigma_x + \sigma_z), \tag{3b}$$

$$n_z \approx n_0 - C_1\sigma_z - C_2(\sigma_x + \sigma_y). \tag{3c}$$

In (3a)–(3c), n_x, n_y, and n_z denote the refractive indices for light polarized along the x-, y-, and z-axes, respectively. The quantity n_0 is the refractive index of the unstressed material, and C_1 and C_2 are the elasto-optic (stress–optic) coefficients. The stress components are σ_x, σ_y, and σ_z, where the subscript indicates the direction of the normal stress.

We modeled the coupled optomechanical response in COMSOL Multiphysics v6.2 (COMSOL AB, Stockholm, Sweden) using a sequential workflow. A 2D axisymmetric solid-mechanics model, using a mesh with free triangular elements, captured the local indentation of a spherical glass tip (radius 11 μm) into a PDMS-on-silicon stack. Contact between the tip and PDMS

Optics EXPRESS

was defined as frictionless, augmented-Lagrangian, surface-to-surface contact. Silicon, silicon dioxide, and the glass tip were modeled as linear, isotropic elastic materials, while PDMS was described by a (Nearly incompressible) Neo-Hookean hyperelastic model. Forces up to 80 µN were applied. The resulting Cauchy principal stress fields in the PDMS and waveguide region were exported to the optical step for computing the stress-induced refractive-index perturbation.

In the next step, 2D optical eigenmode analysis of the waveguide cross-section was performed, incorporating the elasto-optic effect by updating the refractive indices according to (3a)–(3c). The operating wavelength in all simulations was set to $\lambda = 1550$ nm. The effective-index change Δn_{eff} was obtained by carrying out a mode analysis [29], and converted to a resonance wavelength shift through:

$$\Delta\lambda_r \approx \frac{\lambda_r}{n_g}\,\Delta n_{\text{eff}}. \tag{4}$$

Equations (1)–(4) also make clear that the applied load F enters the problem only through the stress field that it generates in the PDMS cladding. For a fixed contact geometry (e.g., spherical tip radius and indentation protocol), standard contact–mechanics models predict a monotonic, but generally nonlinear, dependence of the local stress components on F. Over the limited load range used in this work, our simulations and measurements show that the resulting resonance shift $\Delta\lambda_r(F)$ can be well approximated as linear, which motivates expressing the responsivity in terms of total load. If the contact area or loading configuration is changed, the mapping between F and the local stresses changes accordingly, and the same optomechanical transduction scheme can be used to recalibrate the device for the new geometry.

Lateral selectivity was studied by offsetting the load center relative to the waveguide and repeating the two-step solution.

Table 2 summarizes the material parameters used in the simulations. While birefringence measurements for transparent rubbers at visible wavelengths have been reported in the literature [30], we could not find reliable experimental values of the PDMS stress-optic coefficients C_1 and C_2 at telecom wavelengths. We therefore explored a range of (C_1, C_2) pairs and selected the values that best matched the measured resonance shifts (120 and 70 TPa^{-1}). These values are in the range of thin-film measurements for common polymers [31]. Because C_1 and C_2 were not independently measured, the reported values should be interpreted as fit-based *estimates* for the present device geometry, polarization, and loading condition. In this configuration, the measured resonance shift is governed by a weighted combination of stress components (Eq. (3)), so multiple (C_1, C_2) pairs can provide similar agreement unless additional independent constraints are introduced (e.g., TE/TM interrogation and/or spatially varying load conditions). We therefore use (C_1, C_2) as effective parameters that reproduce the measured calibration curve.

Table 2. Physical constants used in simulation [32–34]

Material	Young's modulus (MPa)	Poisson's ratio	n_o	C_1 (TPa^{-1})	C_2 (TPa^{-1})
PDMS	0.57[a]	0.49	1.396	120[b]	70[b]
Si	110000	0.27	3.476	-17.13	5.51
SiO_2	78000	0.19	1.445	1.17	3.73

[a]Experimentally measured in this study.
[b]Estimated by fitting the coupled FEM-optical model to the measured resonance shifts (see Sec. 2E).

3. Results and discussion

3.1. Modelling of silicon photonic force sensors

Figure 2(a) shows the simulated localized pressure field under a spherical indenter assuming that it is positioned over the center of the MRR with a radius of 4 µm. In the second step, an optical

Optics EXPRESS

eigenmode analysis is performed where the refractive indices are calculated from the mechanical simulations using Eq. (3), showing strong modal confinement in silicon with a measurable evanescent overlap in the PDMS cladding (Fig. 2(b)). This two-step workflow was repeated for applied loads up to 80 μN: the effective index n_{eff} was extracted from the eigenmodes and converted to a resonance shift of the MRR using (4). The resulting calibration (Fig. 2(c)) shows an approximately linear increase of resonance wavelength shift with force, with a representative slope of ~ 71 fm/μN for the geometry studied. At the waveguide centerline, the stress field is dominated by a strongly compressive axial component (σ_z<0), while the X component remains tensile (σ_x>0) and the Y component is at least an order of magnitude smaller. This implies that the C_1- and C_2-weighted contributions enter with opposite sign (partial cancellation), which makes simultaneous extraction of (C_1, C_2) from a single loading dataset potentially challenging.

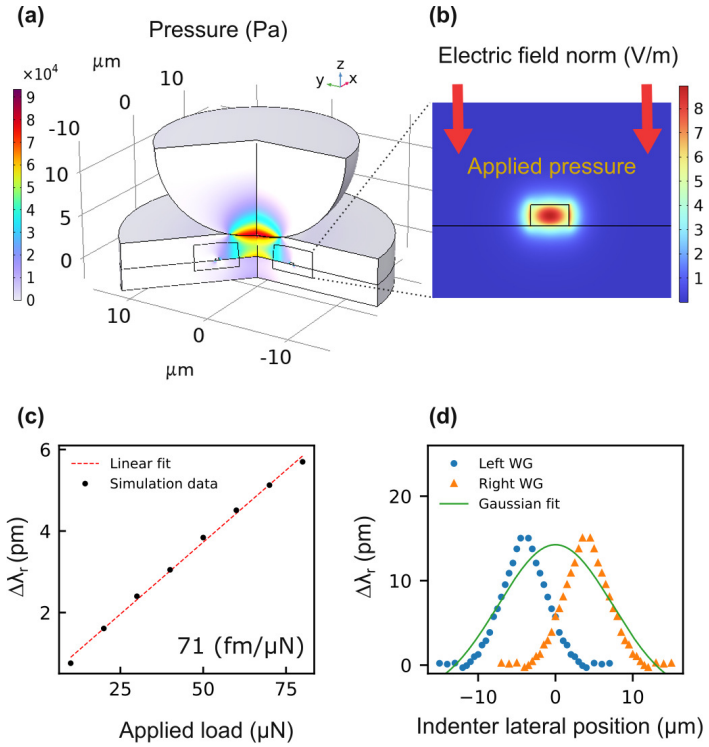

Fig. 2. Simulation of the sensor concept. a) Finite element simulation showing the pressure distribution in the layers under a localized spherical-tip load. b) Simulated waveguide effective index as a function of applied load. c) Calculated resonance shift as a function of applied force and the linear fit (R^2 = 0.99). d) Simulated lateral response: resonance shift versus indenter offset from the center of the ring (X=0) for an applied load of 80 μN. Gaussian fit is applied to the sum of right and left waveguide (WG) response and yields σ = 7.4 ± 0.14, FWHM = 17.4 μm.

In the next step, we laterally translated the indenter relative to the waveguides. The cross-section of a MRR at its center consists of two waveguides separated by its diameter (which is 8 μm in this case). The predicted response (Fig. 2(d)) is spatially confined: the resonance shift decays smoothly with offset and remains detectable out to ~ 5–6 μm from the waveguide center. The Gaussian-like width increases with load, consistent with a larger contact radius and a broader stressed region in the PDMS. As the load grew, the effective-index perturbation extended over a wider area around the waveguide, producing a correspondingly wider response.

Optics EXPRESS

3.2. Single-sensor force calibration

In the experiments, the relative resonance shift was measured as:

$$\text{Relative } \Delta\lambda r = \Delta\lambda_{\text{sense}} - \Delta\lambda_{\text{ref}} \tag{5}$$

where $\Delta\lambda_{\text{sense}}$ and $\Delta\lambda_{\text{ref}}$ are the change in the resonance wavelengths of the sensing and reference rings, respectively. As shown in Fig. 3, the relative resonance shift increases approximately linearly with applied load over the tested range. A linear fit to $\Delta\lambda(F)$ yields a responsivity of $S_{\lambda r} = 66$ fm/μN $\pm$ 8 fm/μN (standard error of the fitted slope), where the uncertainty reflects the spread of slopes obtained from three repeated load–unload cycles and therefore includes both sensor and nanoindenter reproducibility. This is in reasonable agreement with the $\sim$ 71 fm/µN predicted by the elasto–optic model for the fabricated geometry (Fig. 2(c)). Repeated load–unload cycles show consistent slopes with small inter-cycle variation (error bars in Fig. 3(b)), indicating good repeatability.

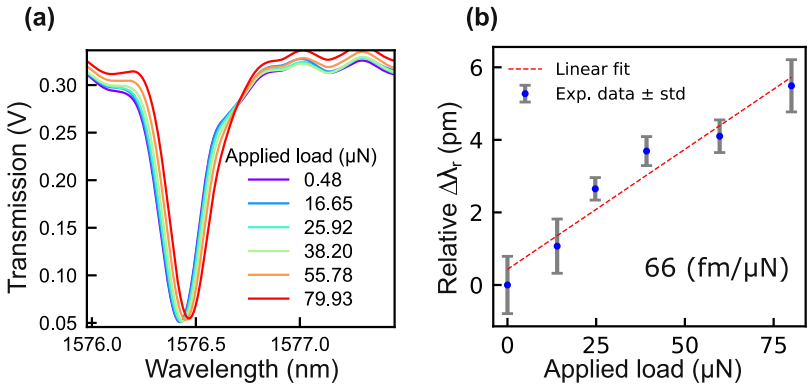

Fig. 3. Experimental validation of the sensor concept. a) Measured transmission spectra of the sensing ring under increasing load. b) Experimental resonance shift (relative to reference ring) vs. load with linear fit ($R^2 = 0.94$). Error bars show standard deviation across 3 independent repetitions at each load.

From the no-load measurements (Fig. S2 of the supplementary document), the wavelength noise floor is $\sigma_\lambda = 0.79$ pm (1σ); with a measured sensitivity $S_{\lambda_r} = 66$ fm/µN, this yields a force resolution $\delta F \approx \sigma_\lambda / S_{\lambda_r} \approx 12$ µN. These values correspond to a single swept-laser acquisition with the settings used in this work. In general, the wavelength noise σ_λ (and thus the force resolution $\delta F \approx \sigma_\lambda / S_{\lambda r}$) scales approximately with the inverse square root of the effective integration time or number of averaged sweeps: averaging over N sweeps improves δF by a factor $\sim 1/\sqrt{N}$ at the expense of a proportional reduction in the effective frame rate, whereas operating at the single-sweep limit maximizes temporal resolution at the cost of higher noise.

The reported wavelength noise floor already includes detector noise, laser jitter and residual drift over the duration of ten minutes. Because the sensing and reference MRRs are interrogated within the same sweep and their resonance shifts are subtracted (Eq. (5)), slow common-mode changes such as laser wavelength drift or ambient temperature variations are largely canceled in $\Delta\lambda_r$. In the present implementation the sweep time and acquisition overhead yield frame times on the order of 1–2 s per row, which is sufficient for tracking cell-generated forces that evolve on time scales of seconds to minutes.

These results establish a stable, temperature-compensated readout with micronewton-scale dynamic range and a force responsivity set by the elasto–optic coupling of the PDMS cladding and the silicon waveguide mode. Across the microrings used in this work we obtain Q values in the range of roughly 5×10^3 to 2.1×10^4, with a median value of about 1.6×10^4. These Q-factors

Optics EXPRESS

are limited by a combination of loss mechanisms, most notably bending loss in the compact microring geometry and absorption and scattering in the PDMS cladding. The elasto–optic transduction coefficient $S_{\lambda r}$ (resonance shift per unit load), by contrast, is primarily determined by the stress distribution in the PDMS and its photoelastic response, and depends only weakly on Q. Increasing Q mainly narrows the resonance linewidth and steepens the transmission slope, which improves the precision with which λ_r can be estimated from a noisy sweep and thus lowers the noise-equivalent force. In other words, a higher Q improves the force *resolution* rather than the intrinsic force-to-wavelength sensitivity. Very high Q would, however, also increase susceptibility to laser-frequency noise and drift unless active resonance locking or referencing is implemented.

3.3. Demonstration of a multiplexed sensor array

To evaluate the spatial resolution and responsiveness of individual microring sensors within the multiplexed array, we chose a five-ring array with 15 μm pitch as shown in Fig. 4(a). Small radius variations are used to spread the ring resonance wavelengths across the spectrum, and enable wavelength-division readout on a single bus (Fig. 4(b)). The leftmost dip is the reference ring used for temperature drift compensation; the remaining dips correspond to sensing rings. The comparable extinction ratio of the dips indicates similar coupling conditions across devices, supporting uniform array behavior.

We performed lateral indentation scans with a pitch of 1 μm over a range of 80 μm. Because the applied load varied slightly between indentations, each response was scaled according to:

$$\mathrm{S}\Delta\lambda_r = (\Delta\lambda_{\mathrm{sense}} - \Delta\lambda_{\mathrm{ref}}) \times \frac{F}{F_{\mathrm{max}}}, \tag{6}$$

where F is the instantaneous load and F_{max} is the maximum load for that indentation. The average applied load across all measurements was 74.3 ± 23.8 μN. Figure 4(c) plots the scaled responses for two sensors located at X = 25 μm (blue) and X = 55 μm (red).

Each sensor exhibits a lateral indentation position at which $\Delta\lambda_r$ peaks, demonstrating its sensitivity to force applied within a defined lateral range. This is consistent with the modeled lateral response of the ring in Fig. 2(d). For an applied load of 80 μN, the two lobes of the waveguide response overlap and turn into a single Gaussian as in Fig. 4(c). By contrast, the peaks from the two different rings (25 μm *vs.* 55 μm) remain well separated, confirming that each ring responds primarily to forces applied above or near its own core.

From a sensing perspective, this position-dependent $\Delta\lambda_r(x, y)$ defines the lateral point-spread function of each pixel and is therefore a designed property rather than a parasitic effect. The ring diameter and array pitch are chosen such that the pixel size and sensitivity width are smaller than typical objects of interest (for example, a single stem cell will cover multiple rings). In this regime, the array is not intended to assign a force to a single isolated pixel, but to monitor how a larger object loads a set of neighbouring sensors, from which the distributed force pattern can be reconstructed. Neglecting this finite lateral response and treating the sensitivity as position independent would mainly introduce systematic errors when forces are applied between pixels or over extended contact areas, leading to underestimation of the local force on a single sensor and apparent responses on neighbouring pixels. Future implementations can combine such per-pixel PSF calibration with standard deconvolution to further reduce reconstruction errors for complex force distributions.

3.4. Demonstration of matrix imaging capabilities

To demonstrate the sensor array's capability to resolve and localize applied forces across a two-dimensional surface, we used a 10×5 microring array with 15 μm pitch (Fig. 5(a). An indenter with a larger spherical tip (radius = 250 μm) was used so that the contact footprint spanned

Optics EXPRESS

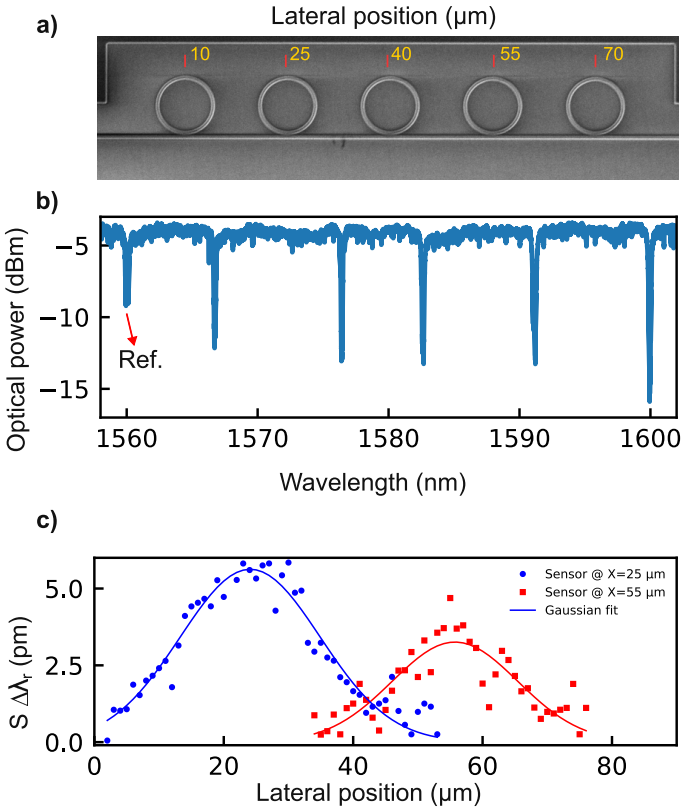

Fig. 4. Demonstration of a multiplexed sensor array. a) SEM image of a section of the array showing five microring resonators coupled to a common bus waveguide; b) Measured optical transmission spectrum showing distinct resonances from rings with slightly different radii; the leftmost dip (arrow) marks the reference ring used for drift compensation. c) Spatial scanning of a nano-indenter tip (radius: 11 μm) across the array in ~ 1 μm steps reveals position-dependent resonance shifts. The relative resonance shift for two selected rings (at x = 25 μm and x = 55 μm) shows distinct peaks. Gaussian fits yield FWHM of = 25.53 and = 22.91 μm for the first and second ring, respectively.

multiple rings. The P1 and P2 circles in the figure indicate the contact areas corresponding to the measurements in Figs. 4(b),(c). The contact radius (a) was estimated by [35]:

$$a = \sqrt{h \times R} \tag{7}$$

where h is the indentation depth and R is the indenter tip radius. The corresponding applied load was approximately 120 μN.

Each ring functions as an independent sensing element, with a dedicated bus waveguide for each row. The force is obtained by dividing the relative wavelength shift by the measured sensitivity. Figure 5(b), c display force heatmaps of the matrix response when the nano-indenter applied force at two different locations. When the indenter is placed near P1, sensors around ($X \approx 5$, $Y \approx 4$) dominate the response (Fig. 5(b); moving the tip to P2 shifts the activated cluster toward ($X \approx 7$, $Y \approx 2$) with minimal overlap between the two patterns. The observed footprint matches the overlaid contact circles, consistent with a localized stress field in the PDMS cladding.

These results show that the response is confined to a few neighboring pixels, confirming that each ring primarily responds to forces applied above or near its core, with limited cross-talk

Optics EXPRESS

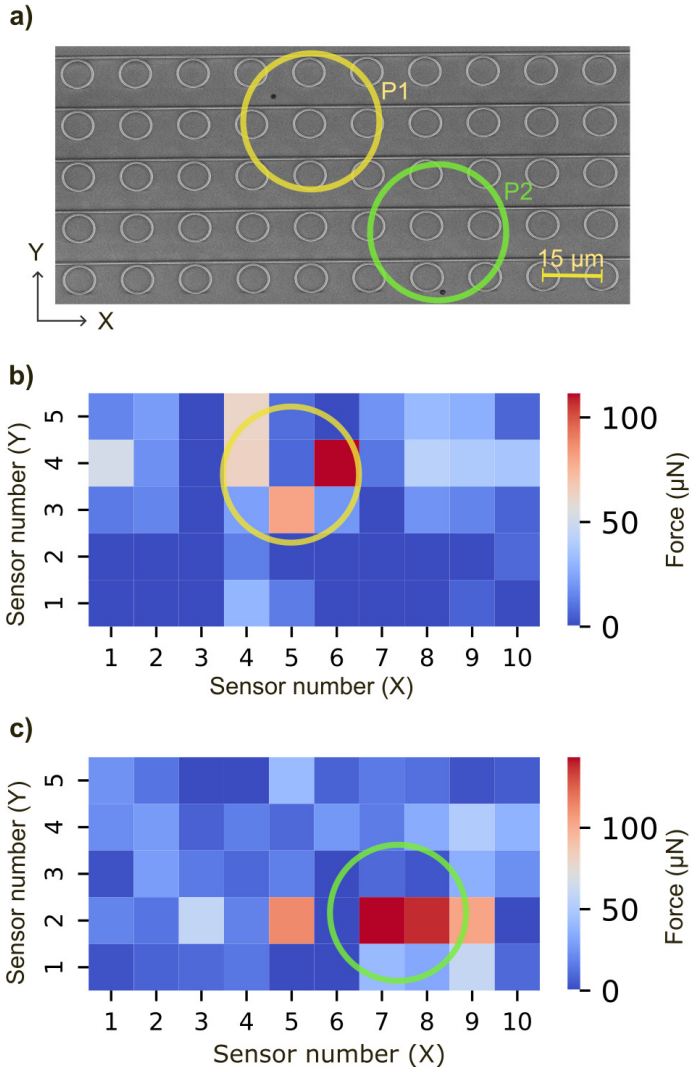

Fig. 5. Matrix force imaging with a 10×5 MRR array and indenter tip radius of 250 µm. (a) SEM of the MRR matrix (sensor indices X and Y) with 15 µm pitch; the yellow (P1) and green (P2) circles mark the estimated nano-indenter contact areas. (b,c) Heatmaps of the force response of each sensor for indentations at P1 and P2, respectively.

Optics EXPRESS

to distant sensors. Considering the FWHM values, for the 15 μm array pitch used here, the response at the centre of a nearest-neighbour pixel is approximately 30–40% of the on-axis response, and falls below $\sim$ 10% beyond two pixels. Expressed in terms of a power ratio, this corresponds to nearest-neighbour crosstalk on the order of -8 to -10 dB and better than -20 dB for sensors separated by more than two pitches. In future work, these experimentally determined point-spread-functions can be assembled into a sensitivity matrix that links the underlying traction field to the vector of measured resonance shifts; standard regularized inverse methods (e.g PSF-based deconvolution) can then be used to reconstruct continuous force fields from the discrete, noisy pixel responses. The map peak or center-of-mass provides a direct estimate of contact location. Because the array is wavelength-multiplexed on a single bus, extending to larger matrices is straightforward; with per-pixel calibration and PSF deconvolution, continuous force fields can be reconstructed in real time. In the present matrix implementation, we switched between rows manually, so the overall acquisition time for a full 10×5 frame was dominated by manual reconfiguration and the quasi-static loading protocol. In a practical instrument, a $1\times N$ fiber-optic switch can sequentially address the rows; typical commercial MEMS-based switches offer millisecond-scale channel switching times, which are negligible compared to the $\sim$ 0.4–0.5 s sweep time per row at a 50 nm/s sweep speed. The temporal resolution for a full array would then be set mainly by the product of the number of rows and the single-row sweep time. Finally, as already noted, resonance locking or multi-line probing can increase frame rates beyond those of swept-laser acquisition while maintaining drift compensation via the reference ring. These findings highlight the potential of this platform for real-time force mapping, especially in applications such as tactile surfaces, robotic skins, or biological systems where forces are distributed across soft tissues or cells. The experiments provide a proof-of-principle demonstration of force mapping. By comparing Figs. 5 (b) and (c) it is however clear that the ring resonator resonance wavelengths of the non-indented MRR are not entirely identical and stable. Also the MRR in the indented regions do not fully follow the expected spherical tip shape. Improving the sensitivity and stability of the MRR sensors is therefore an important next step for increasing the performance and mapping quality of the presented force imaging method. In particular, the apparent force on the pixel closest to the indenter centre in Fig. 5(b) is slightly lower than on its neighbours because the force heatmap is obtained using a single, global sensitivity, while individual rings exhibit small differences in responsivity and baseline stability due to fabrication tolerances, PDMS thickness variations and residual drift. As a result, the cluster position and footprint are reliable indicators of the contact location, whereas the detailed amplitude distribution inside the cluster should not yet be interpreted as a fully quantitative force profile without per-pixel calibration. Two aspects merit further refinement. First, independent calibration of the PDMS stress–optic coefficients at telecom wavelengths would narrow the modeling uncertainties. A brief sensitivity analysis indicates that moderate changes in C_1, C_2 mainly rescale the sensitivity. Second, PDMS viscoelasticity sets time-dependent behavior at higher loads/longer holds; short step–hold–release protocols minimize bias, while future work can incorporate viscoelastic models. Preliminary measurements under cyclic loading, using a fixed-wavelength readout on the resonance flank, show that the sensor can follow dynamic forces on sub-second time scales (Fig. S3 of the supplementary document), although a systematic frequency-response characterization is left for future work. On the instrumentation side, resonance locking or multi-line probing can raise frame rates beyond swept-laser acquisition while maintaining drift cancellation via the reference ring, which would further reduce sensitivity to slow laser drift and enable higher-temporal-resolution studies of evolving cell traction patterns. Finally, denser arrays, application-matched PDMS thickness/formulation, on-chip detection, and microfluidic/biological overlays should extend this approach to real-time force imaging over larger fields with well-defined force resolution $\delta F \approx \sigma_\lambda / S_{\lambda_r}$.

Optics EXPRESS

4. Conclusions

We introduce a polymer–on–silicon photonic force-sensing platform that uses elasto–optic transduction in a thin PDMS cladding layer to convert local surface stress into resonance wavelength shifts of silicon microring resonators. By placing the mechanically compliant, biocompatible material as the cladding, the concept decouples mechanical flexibility from the photonic platform and is intrinsically compatible with dense, planar arrays.

The elasto–optic transduction mechanism is verified experimentally using a calibrated nano-indenter and numerically by FEM simulations. Within the applied load range up to 80 μN the device exhibits an approximately linear response, with a measured responsivity of $S_{\lambda r} = 66 \pm 8$ fm/μN in reasonable agreement with simulations ($\sim$ 71 fm/μN), corresponding to a force resolution down to $\sim$ 12 μN. We demonstrate wavelength-division multiplexing with a linear microring array on a shared bus and two-dimensional force mapping with a 10×5 array at 15 μm pitch. A reference ring positioned outside the stressed region provides effective temperature and common-mode drift compensation, enabling repeated measurements over many loading cycles.

The combination of a soft, bio-compatible cladding, strong opto–mechanical coupling and foundry-compatible silicon photonics establishes a practical route towards scalable, real-time 2D force mapping on flat substrates. The platform is well suited for applications that require micrometer-scale spatial selectivity and multiplexed force readout, including soft-matter metrology, tactile interfaces and in vitro mechanobiology.

Acknowledgement. This work was supported by the TU Delft via the cohesion grant "High-resolution optomechanical sensing for next-generation mechanobiological analysis of cells" awarded to M. J. Mirzaali and W. Westerveld.

Disclosures. The authors declare no conflicts of interest.

Data availability. Data underlying the results presented in this paper are not publicly available at this time but may be obtained from the authors upon request.

Supplemental document. See Supplement 1 for supporting content.

References

1. P. Roca-Cusachs, V. Conte, and X. Trepat, "Quantifying forces in cell biology," Nat. Cell Biol. **19**(7), 742–751 (2017).
2. F. Xia and K. Youcef-Toumi, "Review: advanced Atomic Force Microscopy modes for biomedical research," Biosensors **12**(12), 1116 (2022).
3. L. Schwab, P. E. Allain, N. Mauran, *et al.*, "Very-high-frequency probes for atomic force microscopy with silicon optomechanics," Microsyst. Nanoeng. **8**(1), 32 (2022).
4. C. J. Bustamante, Y. R. Chemla, S. Liu, *et al.*, "Optical tweezers in single-molecule biophysics," Nat. Rev. Methods Primers **1**(1), 25 (2021).
5. B. E. Vos, T. M. Muenker, and T. Betz, "Characterizing intracellular mechanics via optical tweezers-based microrheology," Curr. Opin. Cell Biol. **88**, 102374 (2024).
6. H. Colin-York, D. Shrestha, J. H. Felce, *et al.*, "Super-resolved traction force microscopy (STFM)," Nano Lett. **16**(4), 2633–2638 (2016).
7. A. Zancla, P. Mozetic, M. Orsini, *et al.*, "A primer to traction force microscopy," J. Biol. Chem. **298**(5), 101867 (2022).
8. P. Paulitschke, F. Keber, A. Lebedev, *et al.*, "Ultraflexible nanowire array for label- and distortion-free cellular force tracking," Nano Lett. **19**(4), 2207–2214 (2019).
9. J.-Y. Shiu, L. Aires, Z. Lin, *et al.*, "Nanopillar force measurements reveal actin-cap-mediated YAP mechanotransduction," Nat. Cell Biol. **20**(3), 262–271 (2018).
10. P. Roriz, O. Fraz ao, A. B. Lobo-Ribeiro, *et al.*, "Review of fiber-optic pressure sensors for biomedical and biomechanical applications," J. Biomed. Opt. **18**(5), 050903 (2013).
11. N. Fardian-Melamed, A. Skripka, B. Ursprung, *et al.*, "Infrared nanosensors of piconewton to micronewton forces," Nature **637**(8044), 70–75 (2025).
12. J. R. Casar, C. A. McLellan, C. Shi, *et al.*, "Upconverting microgauges reveal intraluminal force dynamics in vivo," Nature **637**(8044), 76–83 (2025).
13. Q. Zeng, M. Runowski, J. Xue, *et al.*, "Pressure-induced remarkable spectral red-shift in Mn2+-activated NaY9(SiO4)6O2 red-emitting phosphors for high-sensitive optical manometry," Adv. Sci. **11**(9), e2308221 (2024).
14. T.-H. Kim, C.-S. Lee, S. Kim, *et al.*, "Fully stretchable optoelectronic sensors based on colloidal quantum dots for sensing photoplethysmographic signals," ACS Nano **11**(6), 5992–6003 (2017).

Optics EXPRESS

15. N. Quack, A. Y. Takabayashi, H. Sattari, *et al.*, "Integrated silicon photonic MEMS," Microsyst. Nanoeng. **9**(1), 27 (2023).
16. W. J. Westerveld, M. Mahmud-Ul-Hasan, R. Shnaiderman, *et al.*, "Sensitive, small, broadband and scalable optomechanical ultrasound sensor in silicon photonics," Nat. Photonics **15**(5), 341–345 (2021).
17. S. M. Leinders, W. J. Westerveld, J. Pozo, *et al.*, "A sensitive optical micro-machined ultrasound sensor (OMUS) based on a silicon photonic ring resonator on an acoustical membrane," Sci. Rep. **5**(1), 14328 (2015).
18. W. J. Westerveld, J. Pozo, P. J. Harmsma, *et al.*, "Characterization of a photonic strain sensor in silicon-on-insulator technology," Opt. Lett. **37**(4), 479–481 (2012).
19. R. Ravi Kumar, E. Hahamovich, S. Tsesses, *et al.*, "Enhanced sensitivity of silicon-photonics-based ultrasound detection via BCB coating," IEEE Photonics J. **11**(3), 1–11 (2019).
20. Y. Hazan, A. Levi, M. Nagli, *et al.*, "Silicon-photonics acoustic detector for optoacoustic micro-tomography," Nat. Commun. **13**(1), 1488 (2022).
21. M. Nagli, R. Moisseev, N. Suleymanov, *et al.*, "Silicon photonic acoustic detector (SPADE) using a silicon nitride microring resonator," Photoacoustics **32**, 100527 (2023).
22. R. T. Erdogan, G. A. Filonenko, S. J. Picken, *et al.*, "Optimizing cladding elasticity to enhance sensitivity in silicon photonic ultrasound sensors," J. Lightwave Technol. **43**(3), 1419–1428 (2025).
23. I. Turek, N. Tarjányi, I. Martinček, *et al.*, "Effect of mechanical stress on optical properties of polydimethylsiloxane," Opt. Mater. **36**(5), 965–970 (2014).
24. L. Wang, L. Tian, W. Zhang, *et al.*, "Effect of afm nanoindentation loading rate on the characterization of mechanical properties of vascular endothelial cell," Micromachines **11**(6), 562 (2020).
25. M. S. Yousafzai and J. A. Hammer, "Using biosensors to study organoids, spheroids and organs-on-a-chip: a mechanobiology perspective," Biosensors **13**(10), 905 (2023).
26. Y. Peng, N. Yang, Q. Xu, *et al.*, "Recent advances in flexible tactile sensors for intelligent systems," Sensors **21**(16), 5392 (2021).
27. J. J. Ackert, J. K. Doylend, D. F. Logan, *et al.*, "Defect-mediated resonance shift of silicon-on-insulator racetrack resonators," Opt. Express **19**(13), 11969–11976 (2011).
28. P. S. Theocaris and E. E. Gdoutos, *Matrix Theory of Photoelasticity*, vol. 11 of *Springer Series in Optical Sciences*Springer, 1979.
29. T. Fünning, M. Paul, C. L. Manganelli, *et al.*, "Comparative simulation analysis of photonic ultrasound sensors based on silicon waveguides," Sci. Rep. **15**(1), 20094 (2025).
30. A. Angioletti, S. Eccher, O. Polvara, *et al.*, "Rubber birefringence and photoelasticity," Rubber Chem. Technol. **38**(5), 1115–1163 (1965).
31. F. Ay, A. Kocabas, C. Kocabas, *et al.*, "Prism coupling technique investigation of elasto-optical properties of thin polymer films," J. Appl. Phys. **96**(12), 7147–7153 (2004).
32. A. Müller, M. C. Wapler, and U. Wallrabe, "A quick and accurate method to determine the Poisson's ratio and the coefficient of thermal expansion of PDMS," Soft Matter **15**(4), 779–784 (2019).
33. D. J. Lockwood and L. Pavesi, eds.,*Silicon Photonics II: Components and Integration*, vol. 119 of *Topics in Applied Physics*Springer, 2011.
34. S. Tsesses, D. Aronovich, A. Grinberg, *et al.*, "Modeling the sensitivity dependence of silicon-photonics-based ultrasound detectors," Opt. Lett. **42**(24), 5262–5265 (2017).
35. A. C. Fischer-Cripps, *Introduction to Contact Mechanics*, (Springer, 2007), 2nd ed.